How to cite: *Angew. Chem. Int. Ed.* **2024**, *63*, e202408511
doi.org/10.1002/anie.202408511

CO Oxidation | Very Important Paper

Highly Active Oxidation Catalysts through Confining Pd Clusters on CeO_2 Nano-Islands

*Daria Gashnikova, Florian Maurer, Eric Sauter, Sarah Bernart, Jelena Jelic, Paolo Dolcet, Carina B. Maliakkal, Yuemin Wang, Christof Wöll, Felix Studt, Christian Kübel, Maria Casapu, and Jan-Dierk Grunwaldt**

Abstract: CeO_2-supported noble metal clusters are attractive catalytic materials for several applications. However, their atomic dispersion under oxidizing reaction conditions often leads to catalyst deactivation. In this study, the noble metal cluster formation threshold is rationally adjusted by using a mixed CeO_2-Al_2O_3 support. The preferential location of Pd on CeO_2 islands leads to a high local surface noble metal concentration and promotes the *in situ* formation of small Pd clusters at a rather low noble metal loading (0.5 wt %), which are shown to be the active species for CO conversion at low temperatures. As elucidated by complementary *in situ/operando* techniques, the spatial separation of CeO_2 islands on Al_2O_3 confines the mobility of Pd, preventing the full redispersion or the formation of larger noble metal particles and maintaining a high CO oxidation activity at low temperatures. In a broader perspective, this approach to more efficiently use the noble metal can be transferred to further systems and reactions in heterogeneous catalysis.

[*] D. Gashnikova, F. Maurer, P. Dolcet, M. Casapu, J.-D. Grunwaldt
Institute for Chemical Technology and Polymer Chemistry (ITCP)
Karlsruhe Institute of Technology (KIT)
Engesserstraße 20,
76131 Karlsruhe, Germany
E-mail: grunwaldt@kit.edu

S. Bernart, J. Jelic, F. Studt, J.-D. Grunwaldt
Institute of Catalysis Research and Technology (IKFT)
Karlsruhe Institute of Technology (KIT)
Hermann-von-Helmholtz-Platz 1,
76344 Eggenstein-Leopoldshafen, Germany

E. Sauter, Y. Wang, C. Wöll
Institute of Functional Interfaces (IFG)
Karlsruhe Institute of Technology (KIT)
Hermann-von-Helmholtz-Platz 1,
76344 Eggenstein-Leopoldshafen, Germany

C. B. Maliakkal, C. Kübel
Institute of Nanotechnology (INT) and
Karlsruhe Nano Micro Facility (KNMFi)
Karlsruhe Institute of Technology (KIT)
Hermann-von-Helmholtz-Platz 1,
76344 Eggenstein-Leopoldshafen, Germany

C. Kübel
Institute of Materials Research
Technical University Darmstadt (TUDa)
Peter-Grünberg-Straße 2,
64287 Darmstadt, Germany

P. Dolcet
Current address: Department of Chemical Sciences
University of Padova
via Francesco Marzolo 1, 35131 Padova, Italy

Introduction

Highly dispersed noble metals (NMs) supported as single atoms or small particles/clusters on CeO_2 belong to some of the most studied catalytic materials in heterogeneous catalysis. Their unique properties make these systems highly attractive for catalytic applications in the field of mobile and stationary emission control,[1] water-gas shift reaction[2] and electrocatalysis.[3] In comparison to Al_2O_3, CeO_2-supported noble metal oxidation catalysts can overcome CO poisoning at low temperatures,[4] since the CO oxidation reaction can take place at the NM-CeO_2 interface where oxygen is believed to be particularly active.[5] Moreover, ceria stabilizes the NM in a dispersed state by strong NM-ceria interaction, prevents sintering at high temperatures and improves the overall catalyst stability.[6] This is particularly interesting due to the increasing need and limited availability of NMs. However, the strong interaction with ceria often leads to the redispersion of the NM particles under reaction conditions,[7] which can even trigger an activity drop.

In literature, Pt/CeO_2 represents one of the prominent systems for CO oxidation. As recently demonstrated by several studies,[8] atomically dispersed, oxidized Pt species are only poorly active in CO oxidation, despite the highest possible NM-ceria interface and dispersion. Only by applying special pre-treatment and catalyst reactivation procedures leading to the formation of small Pt clusters and nanoparticles the low-temperature activity of such catalysts can be boosted.[6a,8d,9] In contrast to Pt, the active state of Pd/CeO_2 during CO oxidation is still discussed. Whereas some studies reported the oxidized single Pd atoms[10] to be the active species in CO oxidation, others observed a higher activity and stability for Pd clusters[11] or particles.[12] One

recent strategy to circumvent single site formation under oxidizing conditions is by changing the surface noble metal concentration (SNMC),[13] which allows to tune the threshold of noble metal clusters formation. However, too high concentrations of NMs are not ideal in catalytic converters. Therefore, new strategies have to be developed to limit redispersion and/or formation of highly dispersed and inactive species. By using an Al_2O_3 support with a low loading of CeO_2 (around 5.0 wt %), we aim to locally increase the Pd concentration on ceria while keeping the overall NM loading low (0.5–1.0 wt %), an approach visualized in Scheme 1.

To be able to reveal the nature of the active Pd species in CO oxidation, catalyst compositions with different probabilities of cluster formation are prepared by the flame spray pyrolysis (FSP) method. Additionally, a Pd/CeO_2 catalyst with high surface area is obtained, in which the formation of Pd clusters under reaction conditions is hindered due to the high noble metal dispersion on the pure support. Finally, the CO oxidation activity of the ceria-based catalysts is compared to that of a Pd/Al_2O_3 reference sample. By applying complementary *in situ/operando* X-ray and IR-based characterization techniques in combination with DFT calculations, the structural changes occurring during catalyst operation can be tracked for all samples, which allows to determine the active Pd species that are responsible for the high activity of Pd-CeO_2/Al_2O_3 catalyst in the low temperature range, and to tackle the validity of our working hypothesis.

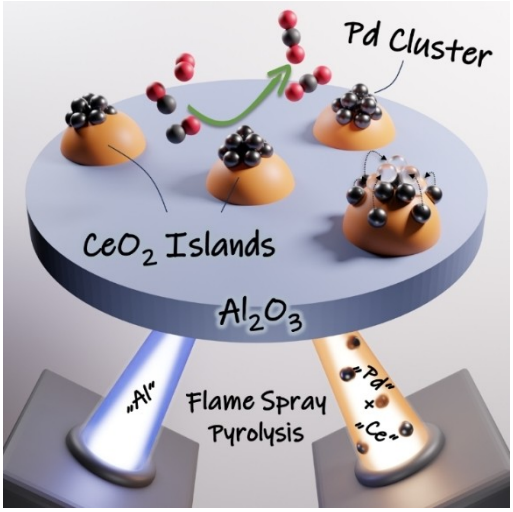

Scheme 1. By using a mixed CeO_2-Al_2O_3 support, the local noble metal (NM) concentration and the probability of cluster formation under reaction conditions can be increased due to the preferential location of Pd on CeO_2 islands. To locate the noble metal on ceria, Pd and Ce precursors are sprayed in one flame separately from the Al precursor in the other flame using double-nozzle flame spray pyrolysis. The spatial separation of CeO_2 entities is thought to prevent Pd from redispersion and strong sintering.

Results and Discussion

To generate Pd-catalysts with high surface area and targeted location of the noble metal, double-nozzle FSP[9] was applied (Scheme 1). As shown previously,[14] the use of the double-nozzle configuration allows preparing complex materials in one single step and fine-tuning the interface between specific catalyst components. This synthetic approach was exploited in our study for the preparation of Pd catalysts supported on pure CeO_2 and Al_2O_3 as well as on a mixed 5 % CeO_2-Al_2O_3 carrier. The preferential location of Pd on CeO_2 in the 0.5 % Pd/5 % CeO_2-Al_2O_3 catalyst was ensured by spraying Pd and CeO_2 precursors in one flame separately from the Al_2O_3 precursor in the other flame. The elemental analysis results confirmed the desired NM loading, while the BET surface area was dependent on the chemical composition of the synthesized catalyst (Table S1). The surface area of 0.5 % Pd/Al_2O_3 amounts to 267 $m^2 g^{-1}$ compared to only 110 $m^2 g^{-1}$ for the 0.5 % Pd/CeO_2 catalyst while the one of 0.5 % Pd/5 % CeO_2-Al_2O_3 is with 239 $m^2 g^{-1}$ between them.

High-angle annular dark-field scanning transmission electron microscopy (HAADF-STEM) images of the resulting samples are shown in Figure 1a–c. In the case of 0.5 % Pd/CeO_2 and 0.5 % Pd/5 % CeO_2-Al_2O_3 (Figure 1a, b), Pd is distributed quite uniformly as very small entities on the ceria support. In the CeO_2-Al_2O_3-based sample, Pd is mostly located on the small ceria nanoparticles, as noble metal rich confined regions (Figure 1b). As expected from the applied synthesis method,[15] due to a short residence time of the precursor solution in the flame, the CeO_2 islands exhibited a small average size (about 2.5 nm, cf. Figure S4). Considering the recent literature,[16] this particular size range of CeO_2 (< 5 nm) and the corresponding redox properties of the Pd-CeO_2 interface are not anticipated to promote CO oxidation under lean conditions over a highly dispersed Pd catalyst. Despite the same low NM loading, small NM nanoparticles with a particle diameter of approx. 2–3 nm were identified by HAADF-STEM and EDXS mapping in the 0.5 % Pd/Al_2O_3 sample (Figure 1c). Particle formation can be explained for this catalyst by the low stabilization of dispersed Pd atoms on Al_2O_3.[17] In line with the electron microscopy data, the corresponding XRD patterns show only reflections of the support material for all catalysts (Figure S2).

As the contrast difference between Pd and CeO_2 in HAADF-STEM is not sufficient to determine the binding geometry and the neighboring environment of Pd on the support surface, additionally *ex situ* XAS data collected at the Pd K-edge were analyzed. For EXAFS analysis, the PdO bulk structure was used together with several DFT-calculated models including Pd located on the CeO_2 surface and Pd substituting one cerium atom on (110) and (111) CeO_2 facets (for details cf. SI, "EXAFS fitting"). The *ex situ* FT-EXAFS spectra of the as-prepared catalysts (Figure 1d–f) confirm the presence of oxidized Pd species in all cases by the prominent first coordination shell at 1.5 Å, which corresponds to Pd-O coordination. The 0.5 % Pd/CeO_2 and 0.5 % Pd/5 % CeO_2-Al_2O_3 catalysts show an additional scattering path at around 2.8 Å that can be assigned to a Pd-O-Ce coordination shell (e.g. R_{eff} = 3.059 Å for 110 PdO-

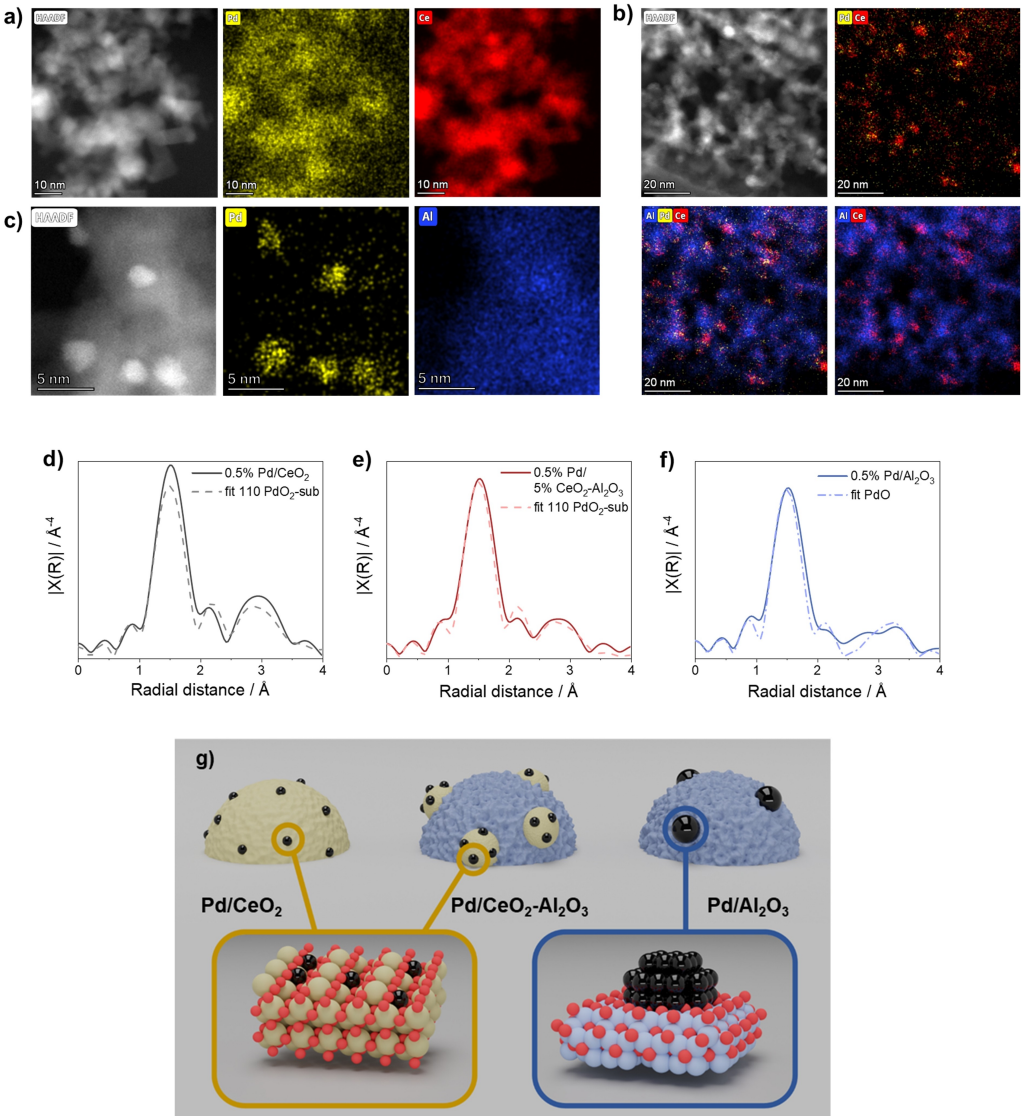

Figure 1. HAADF-STEM images with EDXS elemental maps a) 0.5 % Pd/CeO_2, b) 0.5 % Pd/5 % CeO_2-Al_2O_3 and c) 0.5 % Pd/Al_2O_3 (synthesized by double-nozzle FSP). FT-EXAFS data analysis at the Pd K-edge (experimental data: solid lines; fit: dashed lines), showing the best agreement when using as model: Pd located in four-folded hollow sites, e.g. formally substituted "Pd^{4+}" on (110) facets ("110 PdO_2-sub") for d) 0.5 % Pd/CeO_2 and e) 0.5 % Pd/5 % CeO_2-Al_2O_3, bulk PdO for f) 0.5 % Pd/Al_2O_3. By substituting Ce^{4+} with a Pd atom, a perfect square-planar geometry with Pd-O-Ce bonds is created by the rearrangement of oxygen on the remaining CeO_2 surface, causing a certain charge transfer. While we denote the structure for the EXAFS analysis as "110 PdO_2-sub", a Bader charge analysis suggests that the oxidation state of Pd in this structure is closer to Pd^{2+} (i.e. PdO bulk) rather than Pd^{4+} (i.e. PdO_2 bulk) (Table S5). g) Schematic representation of Pd state in double-nozzle FSP catalysts: highly dispersed Pd in 0.5 % Pd/CeO_2 (left) and 0.5 % Pd/5 % CeO_2-Al_2O_3 (middle) in four-folded hollow sites configuration, small Pd particles in 0.5 % Pd/Al_2O_3 (right). Note the higher local concentration of Pd on CeO_2 in 0.5 % Pd/5 % CeO_2-Al_2O_3 (middle).

sub) or to Pd-O-Pd (R_{eff} = 3.030 Å for PdO). No Pd-Pd scattering path could be identified for both ceria-containing catalysts, which unravels the highly oxidized and well-dispersed Pd species (Tables S6–S8). Furthermore, only poor agreement with experimental data was observed for models with single Pd atoms adsorbed on the (111) and (110) CeO_2 surfaces. Similar to the Pt/CeO_2 system,[8a] Pd seems to be preferentially located at four-fold hollow sites on CeO_2 (Figure S8). This outcome is supported also by studies conducted by Muravev et al.[10b,18] However, it should be noted that the distinction between single atoms and small oxidized clusters is very challenging due to limits of XAS detection. Therefore, the presence of each of these two species cannot be fully excluded.[19] This is further supported by the good agreement of the FT-EXAFS spectrum of 0.5 % Pd/CeO_2 with a fitting model consisting of a combination of bulk PdO and Pd^{2+} substituted into the CeO_2 (111) and (110) surface lattice (Table S7). In contrast, the 0.5 % Pd/Al_2O_3 catalyst shows two contributions with low intensity at around 2.8 and 3.3 Å that correspond to a Pd-O-Pd coordination shell in PdO structure, and indicate the formation of PdO nanoparticles (Table S9).

The catalytic activity of the FSP-prepared catalysts was evaluated for the CO oxidation reaction (1000 ppm of CO,

8 % O_2 in N_2) during three subsequent catalytic cycles. Figure 2a reports the activity obtained during the 2nd light-off between 50 °C and 300 °C. Since all catalysts were tested without a degreening step, a variation in activity was observed for all samples when comparing the 1st run with the next two cycles (Figure S9). The gain in activity observed after the 1st light-off/light-out cycle originates either from removal of adsorbates on the catalyst surface or from resurfacing of partially encapsulated Pd into CeO_2, as reported for other catalysts prepared by FSP.[20]

Among all tested samples, the lowest CO oxidation activity was observed for 0.5 % Pd/CeO_2, for which at 300 °C only 80 % CO is converted. For 0.5 % Pd/Al_2O_3, the reaction sets in at 100 °C, rapidly reaching full conversion below 150 °C. The steep CO conversion profile in comparison to that observed for the CeO_2-containing catalysts probaly originates from a high CO coverage on Pd at low temperatures.[21] Interestingly, 0.5 % Pd/5 % CeO_2-Al_2O_3 exhibits an even higher performance, as indicated by the lowest temperatures of 50 % (T_{50}) and 90 % (T_{90}) CO conversion at 67 and 90 °C, respectively.

As shown in the following, the activity correlates with the different local Pd concentration[13] and evolution of the NM species under reaction conditions in 0.5 % Pd/5 % CeO_2-Al_2O_3 versus 0.5 % Pd/CeO_2. However, the preferential location of Pd species on CeO_2 islands in the 0.5 % Pd/5 % CeO_2-Al_2O_3 sample encompasses also the role of the Pd-CeO_2 interface for the high CO oxidation activity at low temperature. This is in agreement with previous studies,[5a,10b] since CO is fully converted over this sample below 100 °C in comparison to the activity shown by the Pd/Al_2O_3 FSP-catalyst. Similar catalytic behavior was observed with a standard Pd/Al_2O_3 catalyst, prepared by incipient wetness impregnation (Figure S11).

Since Pd and CeO_2 precursors were sprayed in one flame during the preparation of Pd/CeO_2-Al_2O_3 but separately for the Pd/CeO_2 catalyst, the possible influence of the flame configuration was investigated in a first step. A Pd/CeO_2 catalyst with the same chemical composition was prepared *via* the single-nozzle FSP (denoted as 0.5 % Pd/CeO_2-SF). The comparison of the single and double-nozzle FSP catalysts revealed no significant improvement in CO conversion for the first one (Figure S10a). On the contrary, the 0.5 % Pd/CeO_2-SF sample showed an even lower CO oxidation activity (Figure 2b). The partial encapsulation of the NM into the bulk ceria or a higher dispersion of Pd could be possible explanations for the slightly poorer activity measured for the sample obtained with a single-nozzle FSP configuration. To verify the effect of the NM concentration on the ceria surface,[13] a catalyst with a higher Pd loading (1.0 wt %) was synthesized in a single flame configuration. For both single flame prepared catalysts (0.5 % and 1.0 % Pd/CeO_2-SF), *ex situ* characterization results (TEM, XRD, EXAFS) indicate the absence of Pd particles in the as-prepared state (Figures S1–S3). Nonetheless, at the same noble metal weight hourly space velocity of the gas flow, the higher Pd loading led to a slight activity improvement (Figure S10b), shifting the temperature of 90 % CO conversion to 297 °C (Figure 2b). This increase in catalytic performance most probably originates from the more facile formation of Pd clusters, which was found to be important for a high CO oxidation activity on Pt/CeO_2 catalysts.[13]

Finally, the effect of Pd:CeO_2 weight ratio was investigated as a possible descriptor for the CO oxidation activity. A 0.5 % Pd/CeO_2-Al_2O_3 catalyst with a higher CeO_2 content (10 %) was synthesized *via* double-nozzle FSP. With a higher CeO_2 amount and thus lower SNMC, very similar activity profiles were recorded in the low temperature range (Figure 2b and Figure S10c). Though, a slightly higher temperature was needed to reach full CO conversion for the 10 % CeO_2 sample (90 vs. 94 °C), in line with our assumption on the cluster formation probability depending on the Pd concentration on CeO_2 surface.

Hence, by using a carrier material containing a rather low amount of CeO_2 and assisted by a targeted preparation method, the mobility of the NM is significantly restrained. This is additionally demonstrated by the high thermal stability observed upon aging the catalyst in static air at 800 °C for up to 50 h. Thus, only a minor decrease in CO conversion was observed with a difference in the temperature for 50 % conversion of $\Delta T_{50} = 12$ and 23 °C, after aging the 0.5 % Pd/CeO_2-Al_2O_3 catalyst for 5 h and 50 h, respec-

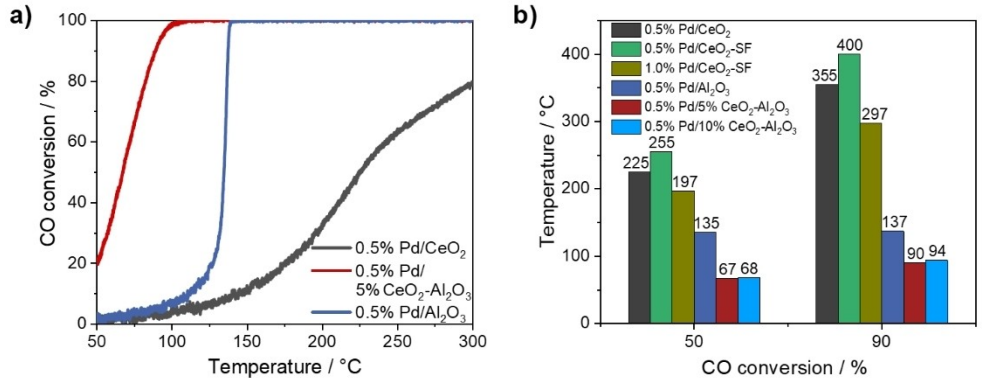

Figure 2. a) Catalytic activity in terms of CO conversion after degreening in 1000 ppm CO/8 % O_2/N_2 of double nozzle-flame synthesized 0.5 % Pd/CeO_2 (grey), 0.5 % Pd/5 % CeO_2-Al_2O_3 (red) and 0.5 % Pd/Al_2O_3 (blue) and b) Overview of temperatures of 50 and 90 % CO conversion for all FSP-synthesized Pd catalysts.

tively (Figure S12). The observed trend is the result of the spatial separation applied in our catalyst. Assuming that all Pd atoms agglomerate to one Pd cluster on each CeO_2 nano-island, a Pd cluster with a maximum of around 30 atoms can be formed during aging in the 0.5 % Pd/5 % CeO_2-Al_2O_3 catalyst (Table S2). Also Li et al.[22] reported a high stability of single-site $Pt/CeO_x/SiO_2$ catalysts due to the strong interaction between Pt and CeO_x. In the same direction, the use of core–shell $Pd@CeO_2$ particles on Al_2O_3 were shown to prevent sintering of the NM particles during methane oxidation.[23] For elucidating the beneficial catalytic behavior of these Pd species, their evolution and reactivity were followed by complementary *in situ* and *operando* methods.

Interaction of Pd with Gaseous CO

To elucidate the nature of the NM species on the catalyst surface and to investigate the available reactive sites as well as their interaction with CO, at first low-temperature, ultra-high vacuum Fourier transform infrared spectroscopy (UHV-FTIRS) measurements using CO as probe molecule were conducted. For this purpose the CO surface-ligand IR (CO-SLIR) method[24] was applied as this surface sensitive approach is well-suited to track the structural evolution of active sites, due to a high sensitivity of the CO stretch vibration to the binding configuration.[25] Due to the inherent problems with adsorbates on nanostructured oxide powders, the Pd/oxide samples were thermally treated prior to the measurements for 1 h at 427 °C in oxygen containing atmosphere (labeled as "cleaned" in Figure 3) or in vacuum, which led to the reduction of Pd species in the catalyst (labeled as "reduced").

The assignment of the observed IR bands was performed based on those reported in the literature[10,18,25a,26] and DFT calculations (Tables S10–S15), as follows: 2130-2120 cm^{-1} (Pd^{2+}-CO, linear), 2095–2085 cm^{-1} ($Pd^{\delta+/0}$-CO, linear) and 1970–1930 cm^{-1} (Pd^0-CO, bridged). In the case of CO bound to Pd subnanometer clusters in a bridged configuration, the agreement between calculated and experimental values improved significantly by considering a higher CO coverage on Pd clusters during DFT calculation (Tables S11–S15). The calculated data are also in line with those reported in literature.[10a,27] According to the DFT calculations, no CO adsorption should be possible on Pd substituting one Ce atom in the (111) and (110) CeO_2 facets (structure derived from experimental EXAFS data of the as-prepared catalysts). In contrast, the CO vibrational frequencies calculated for single Pd atoms adsorbed on these ceria facets (Table S10) showed a good agreement with experimental values in the UHV-FTIR spectra (Figure 3). Hence, we assume that Pd restructures and relocates out of the four-fold hollow sites under UHV-conditions. The high sensitivity of Pd to UHV-conditions is also supported by the X-ray photoelectron spectroscopy (XPS) data (Figure 3d).

To accurately assign the CO adsorbate-related features at approximately 2170 cm^{-1} (R-branch) and 2120 cm^{-1} (P-branch) in the low-resolution IR data (4 cm^{-1}), it is crucial to account for potential artefacts from gas-phase contributions.[28] For this purpose, CO was introduced at low

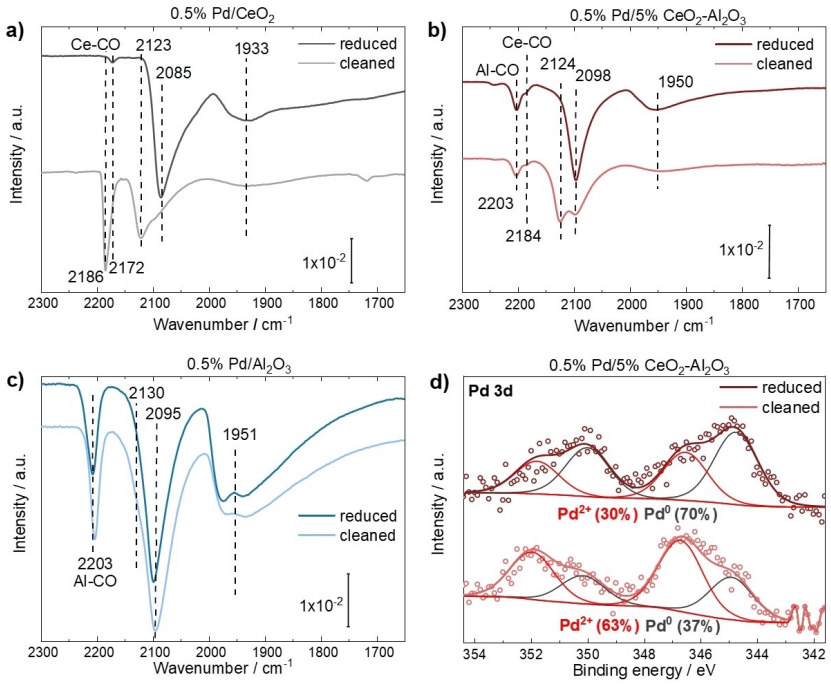

Figure 3. UHV-FTIR spectra recorded at −153 °C in 10^{-3} mbar CO of a) 0.5 % Pd/CeO_2, b) 0.5 % Pd/5 % CeO_2-Al_2O_3 and c) 0.5 % Pd/Al_2O_3 after oxidative cleaning of the surface at 427 °C in 10^{-5} mbar O_2 (cleaned) or in vacuum (10^{-10} mbar) (reduced). The shown spectra are at saturation coverage. d) XPS spectra of 0.5 % Pd/5 % CeO_2-Al_2O_3 taken prior CO adsorption experiments in cleaned and reduced states showing presence of Pd^{2+} (red) and Pd^0 (grey) in the sample.

partial pressures during IR measurements, effectively excluding gas phase interference.

The strong interaction between Pd and ceria as well as the noble metal-induced surface restructuring are further supported by the splitting of the Ce-related CO bands at 2172 and 2186 cm^{-1} (Figure 3a). Whereas the first band was previously observed for pure ceria nanoparticles and attributed to CO bound to Ce^{3+},[29] the band at 2186 cm^{-1} corresponds to CO bound to Ce sites in close proximity to the noble metal substitution sites.[8a,29a] The observed frequency shift is attributed to the modification of chemical environment of surface Ce species. The fact that the oxidized Pd/CeO_2 was dominated by the 2186 cm^{-1} band while this feature was not detected for the reduced Pd/CeO_2 (Figure 3a) provides further evidence for the Pd substitution-induced surface restructuring. The presence of the IR band at 2184 cm^{-1} in the spectra of the reduced and cleaned Pd/CeO_2-Al_2O_3 catalyst (Figure 3b) further confirms the localization of Pd on CeO_2. The IR-band at 2203 cm^{-1} is assigned to CO adsorbed on the Al_2O_3 support.[30]

According to the UHV-FTIRS results, a higher stability of oxidized Pd species was observed for 0.5 % Pd/5 % CeO_2-Al_2O_3 compared to 0.5 % Pd/CeO_2, as indicated by the intensity ratio between the 2130–2120 cm^{-1} (Pd^{2+}-CO) and 2099–2080 cm^{-1} bands ($Pd^{\delta+}$-CO) (Figure 3a–b). Although in both catalysts Pd is present in reduced state after the reductive pre-treatment (427 °C in UHV), the Pd^{2+}-CO species do not vanish completely for 0.5 % Pd/5 % CeO_2-Al_2O_3 (Figure 3b). Moreover, the more prominent band at around 1933 cm^{-1} (bridged CO-Pd^0) implies a stronger NM sintering behavior in the case of 0.5 % Pd/CeO_2. Considering that the same interaction with ceria is present, the milder increase of Pd clusters in the 0.5 % Pd/5 % CeO_2-Al_2O_3 catalyst could be explained by the confined mobility of Pd species on separated CeO_2 islands. Nonetheless, the UHV-FTIR results clearly show the effect of the low partial pressure and low temperature (10^{-3} mbar CO; −153 °C) on Pd reduction in both CeO_2-containing samples.

For the 0.5 % Pd/Al_2O_3 catalyst, the UHV-FTIRS experiments confirmed the presence of larger Pd nanoparticles. Those are expected to be hardly oxidized at a low O_2 pressure in UHV and were easily detected by CO adsorption already during the measurement of the cleaned catalyst (Figure 3c). The predominant IR bands corresponding to bridged (1951 cm^{-1}) and on-top (2095 cm^{-1}) CO adsorbed on Pd nanoparticles or larger clusters were also observed after the reductive pre-treatment.

Prior to the CO adsorption experiments, the oxidation state of Pd was investigated using XPS for the 0.5 % Pd/5 % CeO_2-Al_2O_3 catalyst in cleaned and reduced state (Figure 3d). For the cleaned sample, the spectrum was dominated by the oxidized Pd^{2+} species (63 %), in line with the XAS data analysis showing the presence of highly oxidized and dispersed Pd species in the fresh catalyst state (Figure 1). However, due to high sensitivity of Pd to UHV conditions and the long acquisition time required for this low noble metal-loaded sample, a partial reduction of Pd was induced during the catalyst pre-treatment and the XPS measurement. An even more pronounced reduction of Pd was observed after cleaning of the catalyst surface in vacuum. In this case, the fraction of Pd^{2+} decreased to 40 % according to the quantitative analysis of the XPS data, which further confirms the high sensitivity of Pd to UHV conditions. This behavior is in line with that observed during the CO adsorption with UHV-FTIRS.

Using complementary *in situ* XAS measurements at the Pd K-edge, the interaction and reducibility of Pd was investigated during temperature-programmed reduction (TPR) with CO under ambient pressure. The results of the linear combination analysis (LCA) of the X-ray absorption near edge structure (XANES) spectra are shown in Figure 4a–c (top) for the three Pd catalysts, with the corresponding derivative of Pd_{red} curve (share of reduced species, bottom). According to the LCA results, most of the Pd species in 0.5 % Pd/CeO_2 are rapidly reduced by CO (Figure 4a). The reduction rate peaks at 69 °C, as indicated

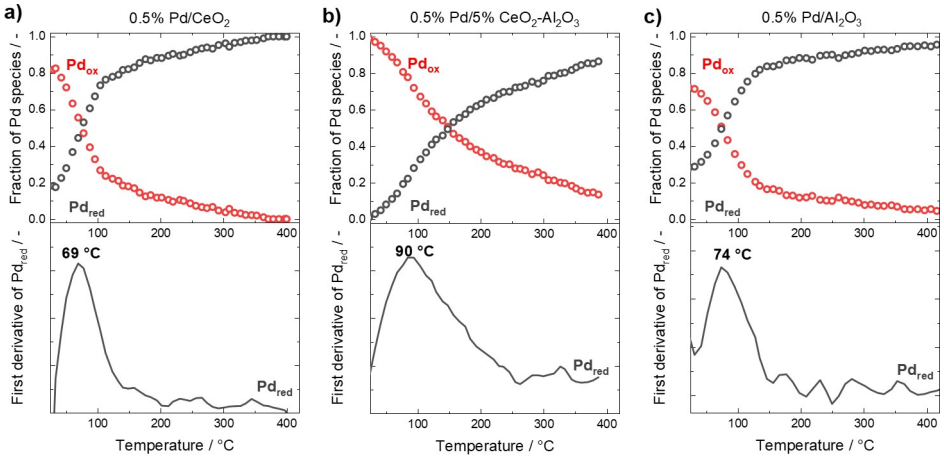

Figure 4. Results of linear combination analysis of X-ray absorption near edge structure (XANES) spectra transiently recorded during CO-temperature-programmed reduction (TPR) in 1000 ppm CO/He with a heating rate of 5 K min^{-1} for double nozzle-flame synthesized a) 0.5 % Pd/CeO_2, b) 0.5 % Pd/5 % CeO_2-Al_2O_3 and c) 0.5 % Pd/Al_2O_3 with a corresponding first derivative of Pd_{red}. Due to large number of data points, the error bars are not shown to ensure clear data visualization. The LCA error is in the range of 1–3 % for all samples.

by the maximum of the first derivative of Pd_{red} curve. In comparison, the intersection of Pd_{ox} and Pd_{red} species is slightly shifted to 74 °C in case of 0.5 % Pd/Al_2O_3 (Figure 4c). Although the reduction of Pd started as soon as the temperature was increased, Pd species in the 0.5 % Pd/5 % CeO_2-Al_2O_3 catalyst remained partially oxidized over a broader temperature window (Figure 4b). In this case, 50 % of reduced species are observed at a significantly higher temperature of 150 °C, with the maximum of reduction rate at 90 °C. A similar reduction trend was observed when the TPR experiments were performed in 2 % H_2/He (Figure S14). In agreement with the UHV-FTIRS, XAS and XPS data discussed above, these results again indicate the presence of Pd species with different nuclearity. Their reactivity under reducing conditions seems to be conditioned by several factors: initial structure, cluster size, interaction with the support (including encapsulation) and interrelated mobility. However, Pd reducibility alone cannot be correlated with the differences in catalytic activity under oxygen-rich conditions of the three catalysts. The 0.5 % Pd/CeO_2 catalyst showed the fastest reduction and pronounced sintering of the NM species in CO atmosphere but still the lowest CO oxidation activity.

Evolution of Pd Sites under Reaction Conditions

To reveal the origin of the activity improvement after the 1st catalytic run, the evolution of Pd species was investigated by *operando* XANES measurements during two consecutive cycles. The LCA results on the changes in Pd oxidation state as a function of CO conversion are depicted in Figure 5 for the three catalysts. In this way, the onset of CO oxidation and the behavior during light-off activity can be directly correlated with the evolving structure of Pd. The activity data obtained during these *operando* XAS experiments are similar to the CO conversion profiles in a laboratory plug-flow reactor (Figure S9).

In contrast to the high redox response observed under reducing conditions (Figure 4a), no significant changes in Pd oxidation state were detected for the 0.5 % Pd/CeO_2 catalyst during both catalytic cycles (Figure 5a). Pd species remain almost fully oxidized over the entire reaction range (only 5 % of Pd is in reduced state at 90 % CO conversion). The Pd supported on 5 % CeO_2-Al_2O_3 was similarly present in an almost fully oxidized state during the 1st catalytic cycle (Figure 5b). However, a slight reduction was observed during the 1st CO oxidation light-out (Figure S15b), and especially a different trend was found during the 2nd run: Pd remained in a partially reduced state (13 % of Pd_{red} at 20 % conversion) and was then slowly reoxidized in reaction atmosphere with the temperature increase. The partial reduction of Pd observed after the 1st catalytic cycle indicates *in situ* cluster formation under reaction conditions. Since these *operando* XANES measurements were conducted at the middle of the catalyst bed, we cannot exclude the presence of slightly more reduced Pd species towards the beginning of the reactor.[4] However, the reduction of the Pd species to their metallic state is rather low under lean reaction conditions, especially considering the small size of these entities and the strong interaction with the CeO_2 support.

In the Pd/Al_2O_3 catalyst the NM is also fully oxidized at the beginning of the 1st catalytic run but already at low CO conversion, a more pronounced reduction of Pd^{2+} species was detected (10 % of Pd_{red} at 20 % conversion) in comparison to the CeO_2-containing samples. The catalyst remained in partially reduced state during the 1st run until 90 % CO conversion, afterwards being reoxidized in the resulting oxygen-rich atmosphere (mid of the catalyst bed). After further reduction during CO oxidation light-out (28 % of Pd_{red}), a similar evolution was noticed for Pd during the second run under reaction conditions (Figure 5c).

Hence, during the lean CO oxidation the low surface Pd concentration as present in 0.5 % Pd/CeO_2 seems to prevent the formation of Pd clusters/particles and NM reduction. In contrast, the *operando* XAS results suggest that partial reduction of Pd species correlates with a high activity at low temperatures, as can be seen in Figure 5b for Pd/CeO_2-Al_2O_3.

To more precisely identify the properties of the NM species responsible for the low temperature activity, complementary DRIFTS measurements were performed during the two consecutive CO oxidation cycles. The spectra acquired

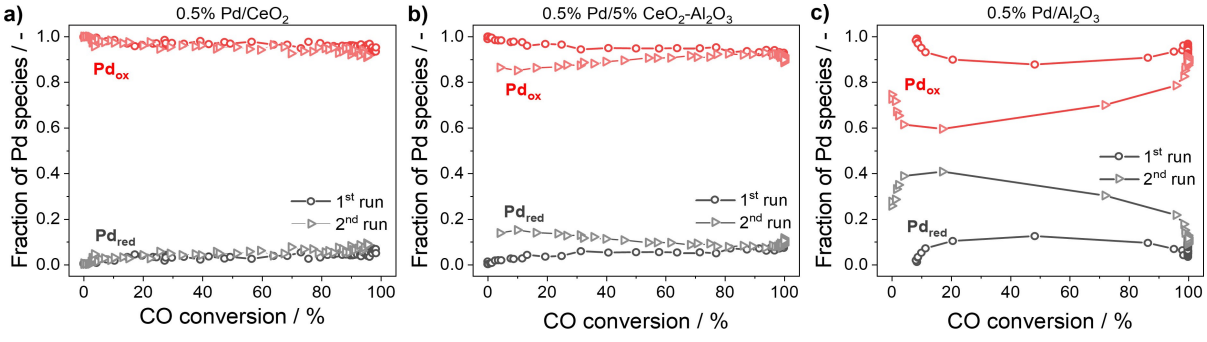

Figure 5. Results of linear combination analysis of XANES spectra transiently recorded at the middle of the catalyst bed during two subsequent catalytic cycles in 1000 ppm CO/10 % O_2/He with a heating rate of 5 K min^{-1} for double nozzle-flame synthesized a) 0.5 % Pd/CeO_2, b) 0.5 % Pd/5 % CeO_2-Al_2O_3 and c) 0.5 % Pd/Al_2O_3. Due to large number of data points, the error bars are not shown to ensure clear data visualization. The LCA error is in the range of 1–3 % for all samples.

every 20 °C up to 110 °C are depicted both for the 1st run (Figure 6a–c) and the 2nd catalytic cycle (Figure 6d–f). For the 0.5 % Pd/CeO_2 catalyst, the DRIFTS data are dominated by a single IR band at 2146 cm^{-1}. A comparison of the DRIFTS results for the 1st and 2nd catalytic cycle revealed only a slight shift of the CO adsorption band to higher wavenumbers from 2143 to 2146 cm^{-1} (Figure 6a, d). Furthermore, a shoulder of very low intensity at ~2100 cm^{-1} was observed during both catalytic cycles. According to literature[10,18,26] and our UHV-FTIRS and DFT calculation results (Figure 3, Tables S10–S15), the IR band at 2143 cm^{-1} corresponds to CO adsorbed on oxidized Pd^{2+} species. In contrast, the band at around 2100 cm^{-1} has been assigned to CO adsorption on several species, including bulk PdO,[31] partially reduced $Pd^{\delta+}$[18] or to highly dispersed Pd^0.[27a] This outlines the challenging task to link the IR bands to specific species if no complementary characterization data are available.[28a] For the sake of simplicity and easier reading, we will refer to this region of the IR spectrum as $Pd^{\delta+}$-CO.

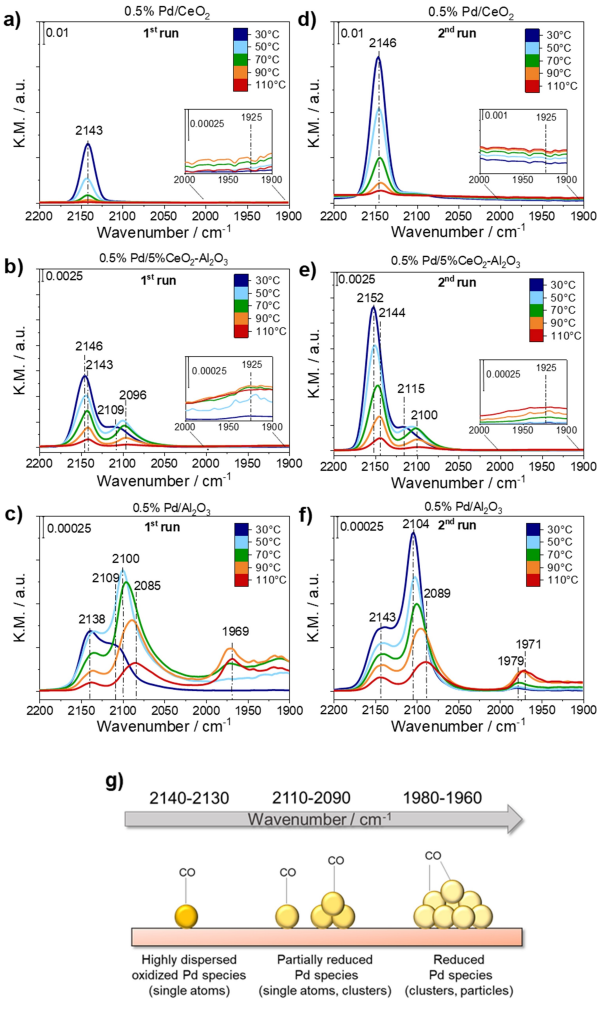

Figure 6. DRIFT spectra recorded during first (a–c) and second catalytic run (d–f) in 1000 ppm CO/10 % O_2/He (200 mL min^{-1}) of double-nozzle flame synthesized 0.5 % Pd/CeO_2 (a, d), 0.5 % Pd/5 % CeO_2-Al_2O_3 (b, e) and 0.5 % Pd/Al_2O_3 (c, f) with graphical representation of IR bands assignment (g).

Based on the electron microscopy and *operando* XAS data (Figure 1a, d, Figure 5a), the Pd/CeO_2 catalyst does not contain PdO nanoparticles, which limits the assignment of the band at around 2100 cm^{-1} to CO adsorbed on highly dispersed $Pd^{\delta+}$ species. This assumption is confirmed by the absence of further bands at lower wavenumbers in the region of bridged CO on multinuclear Pd entities (zoomed view of Figure 6a, d). Hence, under reaction conditions Pd in 0.5 % Pd/CeO_2 remains mostly in an oxidized and highly dispersed state, which is consistent with the LCA results of *operando* XAS data. Additionally, it is important to note that only a very small fraction of CO remains adsorbed on Pd surface at 150 °C during both catalytic cycles (Figure S16), which is not in line with the very low activity recorded for this sample at this temperature (10 % conversion). Similar trends were observed for the pure ceria supported catalysts prepared by single flame-spray pyrolysis (Figure S17a, b, d, e).

Hence, under O_2-rich conditions the partial reduction and the CO-assisted migration of Pd to form larger clusters does not seem to occur on a pure ceria support (Figure 5a). Additionally, the participation of the oxygen from the ceria perimeter sites is not favoured for noble metal single site catalysts.[9] In this case, the reaction seems to proceed *via* a Mars-van-Krevelen mechanism involving reduction/reoxidation of Pd and/or ceria interface with CO and O_2 reacting occurring only at elevated temperatures.

For the 0.5 % Pd/Al_2O_3 catalyst, the DRIFTS data collected at 30 °C prior to the 1st catalytic run (Figure 6c, f, blue) showed a double peak feature at 2138 cm^{-1} (Pd^{2+}-CO) and 2109 cm^{-1} ($Pd^{\delta+}$-CO). While heating in reaction mixture to only 50 °C, the IR band at 2109 cm^{-1} became very prominent and shifted to lower wavenumbers. As stated by Zorn et al.,[32] CO does not adsorb on fully oxidized PdO particles, but rather on substoichiometric PdO_x or metallic Pd species, which are formed under reaction conditions and may lead to the increase in intensity. Furthermore, starting from 70 °C the appearance of a new IR band at 1969 cm^{-1} was observed (Figure 6c). This corresponds to CO adsorbed on the two-fold bridge Pd sites (Pd_2^0-CO),[10a,26a] and confirms significant reduction of Pd species in the catalyst under reaction conditions as observed by the *operando* XAS. Furthermore, it confirms the presence of PdO_x clusters/nanoparticles in the as-prepared catalyst (Figure 1c) or a high mobility of Pd species on the alumina support leading to the formation of reduced Pd nanoparticles. During the 2nd run (Figure 6f), a similar catalyst behavior was obtained. However, around 30–50 °C the weaker IR bands detected in the 1970–1960 cm^{-1} region suggest a certain restructuring of the catalyst under reaction conditions.

In comparison to the 0.5 % Pd/CeO_2 catalyst, the disappearance of the CO adsorption bands at higher temperatures can be clearly correlated to the CO oxidation progress. While the CO adsorbed on two-fold bridged Pd sites appears to be converted in a first stage, the band at 2143 cm^{-1} and especially the one at 2089 cm^{-1} are still visible even when 100 % CO conversion is reached (Figure S16). According to literature (Langmuir–Hinshelwood-mecha-

nism), the reaction ignition occurs when CO coverage on the Pd surface decreases and dissociation of O_2 on Pd can take place, as also indicated by the fast reoxidation of the catalyst at high conversion.[21,33]

The DRIFTS data recorded for the 0.5 % Pd/5 % CeO_2-Al_2O_3 catalyst during the 1st and 2nd run are shown in Figure 6b and Figure 6e, respectively. Analogous to the other samples, the IR bands increased in intensity and were shifted to higher wavenumbers after the 1st catalytic run (Figure 6b vs. 6e). A similar evolution of Pd species under reaction conditions was observed for the sample with higher ceria content (Figure S17c,f). This behaviour could be linked to a higher accessibility of Pd on the surface, which is caused by the CO-induced restructuring of the catalyst under reaction conditions (e.g. partial reduction, resurfacing of encapsulated Pd species). At 30 °C the DRIFT spectrum is dominated by the IR band at 2146 cm^{-1} corresponding to Pd^{2+}-CO species, as observed also for the 0.5 % Pd/CeO_2 catalyst (Figure 6a,d). An additional IR band at 2115 cm^{-1} is present for 0.5 % Pd/5 % CeO_2-Al_2O_3. Due to the high local concentration of Pd on the CeO_2 islands, the *in situ* cluster formation is promoted in this sample compared to the Pd/CeO_2 catalyst. Hence, this feature could correspond to CO adsorption on small PdO_x clusters, as further confirmed by its evolution. With the increase of temperature, this band undergoes a red shift and slightly increases in intensity before it decreases it again above 50 °C. In line with the *operando* XAS data (Figure 5b), this trend indicates partial reduction of Pd species under reaction conditions for Pd on CeO_2 islands, which was not observed for 0.5 % Pd/CeO_2. Furthermore, the formation of partially reduced Pd clusters in the 0.5 % Pd/5 % CeO_2-Al_2O_3 catalyst is indicated by the weak feature appearing above 50 °C in the range of 1980–1900 cm^{-1}, which can be assigned to CO in bridge configuration (Pd_2^0-CO, zoomed view of Figure 6b,e). Analogous to the band characteristic for $Pd^{\delta+}$-CO, this feature further increases and reaches a maximum of its intensity around 100 °C (Figure 6 and Figure S16), suggesting the reaction-induced formation of larger Pd clusters on the expense of highly dispersed species. Hence, when weighting the type of Pd surface species (Figure S16b, e) as derived from the DRIFTS data against the CO oxidation activity (Figure 2) of the CeO_2-based catalyst, the reactivity of PdO_x clusters seems to be superior to that shown by highly dispersed Pd^{2+} species. A similar evolution of the IR bands was observed for the 0.5 % Pd/Al_2O_3 catalyst (Figure S16c,f), although the CO oxidation activity windows are significantly different for the two samples (Figure 2) due to the participation of oxygen provided from ceria to the reaction mechanism.

As summarized in Scheme 2, by using FSP in a double flame configuration we were able to prepare high surface area Pd-based catalysts supported on CeO_2, Al_2O_3 and CeO_2-Al_2O_3 with different abilities of cluster/particle formation. According to *ex situ* characterization results, Pd is present in a highly dispersed, oxidized state in 0.5 % Pd/CeO_2 and 0.5 % Pd/5 % CeO_2-Al_2O_3, whereas in the 0.5 % Pd/Al_2O_3 sample oxidized PdO particles of 2–3 nm are obtained. The catalytic activity was lowest for the 0.5 % Pd/CeO_2 catalyst, which reached 90 % CO conversion only at

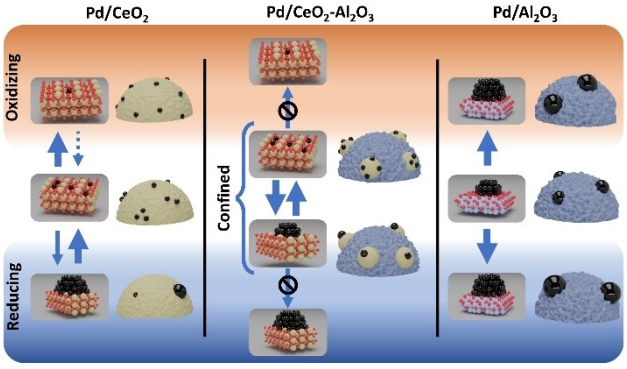

Scheme 2. Schematic representation of the Pd confinement approach for the Pd/CeO_2-Al_2O_3 catalyst. A higher concentration of Pd on CeO_2 in the Pd/CeO_2-Al_2O_3 catalyst facilitates cluster formation under reducing conditions whereas a spatial separation of CeO_2 entities restricts the redispersion process in oxidizing/lean reaction atmosphere. On the contrary, both redispersion and sintering processes cannot be prevented for the Pd/CeO_2 sample due to high dispersion and mobility of Pd on the support. For a pure Al_2O_3 carrier, larger Pd nanoparticles are observed under both conditions (blue: Al_2O_3, CeO_2: yellow; Pd/PdO: black).

355 °C. In this case, the weaker adsorption of CO on Pd single sites combined with rather inactive ceria perimeter sites (low oxygen availability) seems to hinder CO conversion at low temperatures. When supported on alumina, Pd is present as larger clusters and nanoparticles that are partially reduced under reaction conditions. They strongly adsorb CO which leads to self-inhibition at low temperatures with the reaction onset only above 100 °C and full CO conversion at around 140 °C.

In contrast, the 0.5 % Pd/5 % CeO_2-Al_2O_3 catalyst fully converts CO at a realistic gas hourly space velocity already at 90 °C without any activation pre-treatment. In this case, the formation of small PdO_x clusters due to the higher local surface concentration and confinement of Pd on the ceria islands (Scheme 2, middle) is the driving factor for a high catalytic activity during CO oxidation at low temperatures. Equally important seems to be the participation of the oxygen at the interface with ceria to the reaction mechanism, in a similar way as previously demonstrated for Pt/CeO_2-based catalysts.[4a]

Conclusion

In this work, the threshold of noble metal cluster formation could be tailored in CeO_2-based catalysts by using CeO_2 nano-islands on Al_2O_3 as support. Despite the low noble metal loading, the 0.5 % Pd-CeO_2/Al_2O_3 catalyst shows an outstanding CO oxidation activity and stability. The purpose of the mixed CeO_2-Al_2O_3 support relies on a local increase of the NM concentration (up to 30 atoms per CeO_2 island) that facilitates the *in situ* formation of small PdO_x clusters under reaction conditions at low temperatures in contrast to the Pd/CeO_2 and Pd/Al_2O_3 counterparts. By means of flame spray pyrolysis, Pd and CeO_2 precursors were sprayed

separately from the Al_2O_3 precursor during the preparation of 0.5 % Pd/5 % CeO_2-Al_2O_3. This approach ensures a preferential location of Pd on CeO_2 and thus a close NM-ceria contact.

Under reducing conditions, complementary *in situ* XAS and UHV-FTIR spectroscopy uncovered that both the highly dispersed Pd single sites on CeO_2 as well as the Pd clusters on Al_2O_3 are easily reduced and migrate to form larger entities. However, a different behavior was observed during CO oxidation. Despite a similar initial state, Pd supported on pure CeO_2 remained oxidized during the catalytic cycles, while a partial reduction was observed for the NM species in Pd/CeO_2-Al_2O_3, as uncovered by *operando* XAS and DRIFTS. Partial reduction of Pd species was also observed on alumina but, according to DRIFTS this is accompanied by fast reduction and formation of larger Pd entities. This seems to be prevented in ceria-based catalysts, where the interaction with ceria and the oxygen at the perimeter sites further help to circumvent CO inhibition at low temperatures.

The correlation of the characterization results with the catalytic activity data therefore revealed the major importance of small PdO_x clusters on ceria in combination with the active Pd-CeO_2 interface for a high low-temperature CO oxidation activity. Their spatial separation, as achieved by supporting Pd/CeO_2 on Al_2O_3, confines the mobility of Pd and hinders the strong sintering or redispersion during long operation periods, as further demonstrated by the high stability under thermal aging conditions. Thus, the confinment of a defined number of NM atoms on CeO_2 nanoislands represents a promising approach for future development of custom-designed catalysts with reduced NM loading. By using a combination of two differently interacting metal oxides and by exploiting the strong noble metal-support interaction, this concept of controlled agglomeration and limited redispersion can also be transferred to further catalytic systems (e.g. other NMs, further oxide islands) and reactions.

Supporting Information

The data that support the findings of this study are available in the Supporting Information of this article. The authors have cited additional references within the Supporting Information.[34–39]

Acknowledgements

D.G. acknowledges the "Fonds der Chemischen Industrie" (FCI) of the Verband der Chemischen Industrie e.V. (VCI) for financial support during her Ph.D. studies. This study was further funded by the Deutsche Forschungsgemeinschaft (DFG, German Research Foundation) – SFB 1441 – Project-ID 426888090 (projects A3/B1, A4, B2, B3, B4). The authors acknowledge the KIT Light Source for beamtime at the CAT-ACT beamline and SOLEIL at the SAMBA beamline (Saint-Aubin, France) with kind support by A. Zitolo, G. Alizon and L. Barthe. Electron microscopy was supported by the Karlsruhe Nano Micro Facility (KNMFi), a Helmholtz Research Infrastructure at KIT. The authors acknowledge X. Huang for the STEM measurements shown in Figure 1b and D. Wang for discussion of STEM results. We thank A. Zimina (IKFT, KIT) for the measurements of *ex situ* samples and T. Delrieux, M. Maurer, D. Zengel and S. Barth (ITCP, IKFT, KIT) for assistance during the *in situ* XAS experiments. T. Bergfeldt (IAM-AWP, KIT) is acknowledged for ICP-OES analysis and M. Makowiak (IKFT, KIT) for BET measurements. The authors acknowledge support by the state of Baden-Württemberg through bwHPC and the German Research Foundation (DFG) through grant no. INST 40/575-1 FUGG (JUSTUS2, RVs bw17D011). Open Access funding enabled and organized by Projekt DEAL.

Conflict of Interest

The authors declare no conflict of interest.

Data Availability Statement

The data that support the findings of this study are available in KITopen at http://doi.org/10.35097/PvkiykxrYcyhDLeP.

Keywords: ceria · cluster formation · noble metal confinement · operando · palladium

[1] a) S. Rood, S. Eslava, A. Manigrasso, C. Bannister, *Proc. Inst. Mech. Eng. D: J. Automob. Eng.* **2020**, *234*, 936–949; b) L. Liu, A. Corma, *Chem. Rev.* **2018**, *118*, 4981–5079; c) X. Li, X. Yang, Y. Huang, T. Zhang, B. Liu, *Adv. Mater.* **2019**, *31*, 1902031.

[2] T. Montini, M. Melchionna, M. Monai, P. Fornasiero, *Chem. Rev.* **2016**, *116*, 5987–6041.

[3] a) L. Adijanto, A. Sampath, A. S. Yu, M. Cargnello, P. Fornasiero, R. J. Gorte, J. M. Vohs, *ACS Catal.* **2013**, *3*, 1801–1809; b) H. A. Miller, M. Bellini, D. R. Dekel, F. Vizza, *Electrochem. Commun.* **2022**, *135*, 107219.

[4] a) A. M. Gänzler, M. Casapu, D. E. Doronkin, F. Maurer, P. Lott, P. Glatzel, M. Votsmeier, O. Deutschmann, J.-D. Grunwaldt, *J. Phys. Chem. Lett.* **2019**, *10*, 7698–7705; b) A. M. Gänzler, M. Casapu, A. Boubnov, O. Müller, S. Conrad, H. Lichtenberg, R. Frahm, J.-D. Grunwaldt, *J. Catal.* **2015**, *328*, 216–224.

[5] a) M. Cargnello, V. V. Doan-Nguyen, T. R. Gordon, R. E. Diaz, E. A. Stach, R. J. Gorte, P. Fornasiero, C. B. Murray, *Science* **2013**, *341*, 771–773; b) Y. Lu, C. Thompson, D. Kunwar, A. K. Datye, A. M. Karim, *ChemCatChem* **2020**, *12*, 1726–1733.

[6] a) A. M. Gänzler, M. Casapu, P. Vernoux, S. Loridant, F. J. Cadete Santos Aires, T. Epicier, B. Betz, R. Hoyer, J.-D. Grunwaldt, *Angew. Chem. Int. Ed.* **2017**, *56*, 13078–13082; b) J. Lee, Y. Ryou, X. Chan, T. J. Kim, D. H. Kim, *J. Phys. Chem. C* **2016**, *120*, 25870–25879.

[7] a) J. Jones, H. Xiong, A. T. DeLaRiva, E. J. Peterson, H. Pham, S. R. Challa, G. Qi, S. Oh, M. H. Wiebenga, X. I. Pereira Hernández, *Science* **2016**, *353*, 150–154; b) B. B. Sarma,

F. Maurer, D. E. Doronkin, J.-D. Grunwaldt, *Chem. Rev.* **2023**, *123*, 379–444.
[8] a) F. Maurer, J. Jelic, J. Wang, A. Gänzler, P. Dolcet, C. Wöll, Y. Wang, F. Studt, M. Casapu, J.-D. Grunwaldt, *Nat. Catal.* **2020**, *3*, 824–833; b) G. Ferré, M. Aouine, F. Bosselet, L. Burel, F. J. C. S. Aires, C. Geantet, S. Ntais, F. Maurer, M. Casapu, J.-D. Grunwaldt, *Catal. Sci. Technol.* **2020**, *10*, 3904–3917; c) S. Gatla, D. Aubert, G. Agostini, O. Mathon, S. Pascarelli, T. Lunkenbein, M. G. Willinger, H. Kaper, *ACS Catal.* **2016**, *6*, 6151–6155; d) D. Kunwar, S. Zhou, A. DeLaRiva, E. J. Peterson, H. Xiong, X. I. Pereira-Hernández, S. C. Purdy, R. ter Veen, H. H. Brongersma, J. T. Miller, H. Hashiguchi, L. Kovarik, S. Lin, H. Guo, Y. Wang, A. K. Datye, *ACS Catal.* **2019**, *9*, 3978–3990; e) X. I. Pereira-Hernández, A. DeLaRiva, V. Muravev, D. Kunwar, H. Xiong, B. Sudduth, M. Engelhard, L. Kovarik, E. J. Hensen, Y. Wang, *Nat. Commun.* **2019**, *10*, 1358; f) J. Resasco, L. DeRita, S. Dai, J. P. Chada, M. Xu, X. Yan, J. Finzel, S. Hanukovich, A. S. Hoffman, G. W. Graham, S. R. Bare, X. Pan, P. Christopher, *J. Am. Chem. Soc.* **2020**, *142*, 169–184.
[9] A. M. Gänzler, M. Casapu, F. Maurer, H. Störmer, D. Gerthsen, G. r Ferré, P. Vernoux, B. Bornmann, R. Frahm, V. Murzin, *ACS Catal.* **2018**, *8*, 4800–4811.
[10] a) G. Spezzati, Y. Su, J. P. Hofmann, A. D. Benavidez, A. T. DeLaRiva, J. McCabe, A. K. Datye, E. J. Hensen, *ACS Catal.* **2017**, *7*, 6887–6891; b) V. Muravev, G. Spezzati, Y.-Q. Su, A. Parastaev, F.-K. Chiang, A. Longo, C. Escudero, N. Kosinov, E. J. Hensen, *Nat. Catal.* **2021**, *4*, 469–478.
[11] a) H. Jeong, O. Kwon, B.-S. Kim, J. Bae, S. Shin, H.-E. Kim, J. Kim, H. Lee, *Nat. Catal.* **2020**, *3*, 368–375; b) R. Gulyaev, A. Stadnichenko, E. Slavinskaya, A. Ivanova, S. Koscheev, A. Boronin, *Appl. Catal. A* **2012**, *439*, 41–50.
[12] S. Hinokuma, H. Fujii, M. Okamoto, K. Ikeue, M. Machida, *Chem. Mater.* **2010**, *22*, 6183–6190.
[13] F. Maurer, A. Beck, J. Jelic, W. Wang, S. Mangold, M. Stehle, D. Wang, P. Dolcet, A. M. Gänzler, C. Kübel, *ACS Catal.* **2022**, *12*, 2473–2486.
[14] a) M. Høj, D. K. Pham, M. Brorson, L. Mädler, A. D. Jensen, J.-D. Grunwaldt, *Catal. Lett.* **2013**, *143*, 386–394; b) M. Minnermann, H. K. Grossmann, S. Pokhrel, K. Thiel, H. Hagelin-Weaver, M. Bäumer, L. Mädler, *Catal. Today* **2013**, *214*, 90–99.
[15] H. K. Grossmann, T. Grieb, F. Meierhofer, M. Hodapp, D. Noriler, A. Gröhn, H. Meier, U. Fritsching, K. Wegner, L. Mädler, *J. Nanopart. Res.* **2015**, *17*, 1–16.
[16] V. Muravev, A. Parastaev, Y. van den Bosch, B. Ligt, N. Claes, S. Bals, N. Kosinov, E. J. Hensen, *Science* **2023**, *380*, 1174–1179.
[17] E. J. Peterson, A. T. DeLaRiva, S. Lin, R. S. Johnson, H. Guo, J. T. Miller, J. H. Kwak, C. H. Peden, B. Kiefer, L. F. Allard, *Nat. Commun.* **2014**, *5*, 4885.
[18] V. Muravev, J. F. Simons, A. Parastaev, M. A. Verheijen, J. J. Struijs, N. Kosinov, E. J. Hensen, *Angew. Chem. Int. Ed.* **2022**, *61*, e202200434.
[19] J. Finzel, K. M. Sanroman Gutierrez, A. S. Hoffman, J. Resasco, P. Christopher, S. R. Bare, *ACS Catal.* **2023**, *13*, 6462–6473.
[20] a) N. J. Pineau, S. D. Keller, A. T. Güntner, S. E. Pratsinis, *Microchim. Acta* **2020**, *187*, 96; b) N. van Vegten, M. Maciejewski, F. Krumeich, A. Baiker, *Appl. Catal. B* **2009**, *93*, 38–49.
[21] E. K. Dann, E. K. Gibson, C. R. A. Catlow, V. Celorrio, P. Collier, T. Eralp, M. Amboage, C. Hardacre, C. Stere, A. Kroner, *J. Catal.* **2019**, *373*, 201–208.
[22] X. Li, X. I. Pereira-Hernández, Y. Chen, J. Xu, J. Zhao, C.-W. Pao, C.-Y. Fang, J. Zeng, Y. Wang, B. C. Gates, *Nature* **2022**, *611*, 284–288.
[23] M. Cargnello, J. D. Jaén, J. H. Garrido, K. Bakhmutsky, T. Montini, J. C. Gámez, R. Gorte, P. Fornasiero, *Science* **2012**, *337*, 713–717.
[24] C. Wöll, *ACS Catal.* **2020**, *10*, 168–176.
[25] a) S. Liu, Y. Li, X. Yu, S. Han, Y. Zhou, Y. Yang, H. Zhang, Z. Jiang, C. Zhu, W. Li, C. Wöll, Y. Wang, W. Shen, *Nature Commun.* **2022**, *13*, 4559; b) A. Chen, X. Yu, Y. Zhou, S. Miao, Y. Li, S. Kuld, J. Sehested, J. Liu, T. Aoki, S. Hong, M. F. Camellone, S. Fabris, J. Ning, C. Jin, C. Yang, A. Nefedov, C. Wöll, Y. Wang, W. Shen, *Nat. Catal.* **2019**, *2*, 334–341; c) C. Yang, M. Capdevila-Cortada, C. Dong, Y. Zhou, J. Wang, X. Yu, A. Nefedov, S. Heißler, N. López, W. Shen, C. Wöll, Y. Wang, *J. Phys. Chem. Lett.* **2020**, *11*, 7925–7931.
[26] a) G. Spezzati, A. D. Benavidez, A. T. DeLaRiva, Y. Su, J. P. Hofmann, S. Asahina, E. J. Olivier, J. H. Neethling, J. T. Miller, A. K. Datye, *Appl. Catal. B* **2019**, *243*, 36–46; b) B. B. Sarma, J. Jelic, D. Neukum, D. E. Doronkin, X. Huang, F. Studt, J.-D. Grunwaldt, *J. Phys. Chem. C* **2023**, *127*, 3032–3046.
[27] a) D. Jiang, G. Wan, C. E. García-Vargas, L. Li, X. I. Pereira-Hernández, C. Wang, Y. Wang, *ACS Catal.* **2020**, *10*, 11356–11364; b) H. Unterhalt, G. Rupprechter, H.-J. Freund, *J. Phys. Chem. B* **2002**, *106*, 356–367.
[28] a) F. C. Meunier, *J. Phys. Chem. C* **2021**, *125*, 21810–21823; b) L. Caulfield, E. Sauter, H. Idriss, Y. Wang, C. Wöll, *J. Phys. Chem. C* **2023**, *127*, 1875–1932.
[29] a) J. Wang, E. Sauter, A. Nefedov, S. Heißler, F. Maurer, M. Casapu, J.-D. Grunwaldt, Y. Wang, C. Wöll, *J. Phys. Chem. C* **2022**, *126*, 9051–9058; b) C. Yang, X. Yu, S. Heißler, A. Nefedov, S. Colussi, J. Llorca, A. Trovarelli, Y. Wang, C. Wöll, *Angew. Chem. Int. Ed.* **2017**, *56*, 375–379.
[30] a) C. Morterra, G. Magnacca, *Catal. Today* **1996**, *27*, 497–532; b) J. N. Kondo, R. Nishitani, E. Yoda, T. Yokoi, T. Tatsumi, K. Domen, *Phys. Chem. Chem. Phys.* **2010**, *12*, 11576–11586.
[31] F. Zhang, L. Pan, T. Li, J. T. Diulus, A. Asthagiri, J. F. Weaver, *J. Phys. Chem. C* **2014**, *118*, 28647–28661.
[32] K. Zorn, S. Giorgio, E. Halwax, C. R. Henry, H. Grönbeck, G. Rupprechter, *J. Phys. Chem. C* **2011**, *115*, 1103–1111.
[33] a) M. Haneda, M. Todo, Y. Nakamura, M. Hattori, *Catal. Today* **2017**, *281*, 447–453; b) E. Slavinskaya, O. Stonkus, R. Gulyaev, A. Ivanova, V. Zaikovskii, P. Kuznetsov, A. Boronin, *Appl. Catal. A* **2011**, *401*, 83–97.
[34] W. Y. Teoh, R. Amal, L. Mädler, *Nanoscale* **2010**, *2*, 1324–1347.
[35] S. Brunauer, P. H. Emmett, E. Teller, *J. Am. Chem. Soc.* **1938**, *60*, 309–319.
[36] A. Zimina, K. Dardenne, M. Denecke, D. Doronkin, E. Huttel, H. Lichtenberg, S. Mangold, T. Pruessmann, J. Rothe, T. Spangenberg, *Rev. Sci. Instrum.* **2017**, *88*, 113113.
[37] C. La Fontaine, S. Belin, L. Barthe, O. Roudenko, V. Briois, *Synchrotron Radiat. News* **2020**, *33*, 20–25.
[38] F. C. Meunier, *Chem. Soc. Rev.* **2010**, *39*, 4602–4614.
[39] a) Y. Wang, A. Glenz, M. Muhler, C. Wöll, *Rev. Sci. Instrum.* **2009**, *80*, 113108; b) Y. Wang, C. Wöll, *Chem. Soc. Rev.* **2017**, *46*, 1875–1932.

Manuscript received: May 5, 2024
Accepted manuscript online: June 15, 2024
Version of record online: July 17, 2024